Supporting Information

Constructing heterolytic cleavage process of water on Ni_3N nanosheets through single transition metal doping for ultra-efficient alkaline hydrogen evolution

Wansen Ma [a], Meng Wang [a], Chaowen Tan [a], Jiancheng Wang [b], Yanan Dai [b], Liwen Hu [a], Xuewei Lv [a], Qian Li [c,d], Jie Dang [a,*]

[a] College of Materials Science and Engineering, Chongqing Key Laboratory of Vanadium-Titanium Metallurgy and New Materials, Chongqing University, Chongqing, 400044, PR China

[b] Weiqiao-UCAS Science and Technology Park, Binzhou, Shandong Province, 256606, PR China

[c] National Engineering Research Center for Magnesium Alloys, Chongqing University, Chongqing, 400044, PR China

[d] State Key Laboratory of Advanced Special Steels & Shanghai Key Laboratory of Advanced Ferrometallurgy, School of Materials Science and Engineering, Shanghai University, Shanghai, 200444, PR China

***Corresponding author:**

Jie Dang

E-mail: jiedang@cqu.edu.cn

Phone: +86-23-65112631; Fax: +86-23-65112631

Address: College of Materials Science and Engineering, Chongqing University, Chongqing 400044, PR China

Jie Dang ORCID: https://orcid.org/0000-0003-1383-8390

Wansen Ma and Meng Wang contributed equally.

Experimental section

Synthesis of M-doped nanosheets: V-doped nanosheets were prepared on nickel foam via a two-step method. Firstly, nickel foam substrate was pretreated with 3M HCl to remove the oxide layer and impurity on the surface, and then cleaned by deionized water and ethanol for several times. Secondly, nickel foam supported vanadium doped nickel hydroxide nanosheets were synthesized by a modified hydrothermal reaction. Typically, 0.05 mmol NH_4VO_3, 0.95 mmol $Ni(CH_3COO)_2{\cdot}4H_2O$, 5 mmol of $CO(NH_2)_2$ and 2 mmol NH_4F were dissolved in 20 mL deionized water under stirring to form a homogeneous solution. The solution and a piece of nickel foam (NF, 2cm*3cm) were transferred into a 50 mL Teflon-lined autoclave, sealed and kept at 120 ℃ for 4h, to obtain vanadium doped nickel hydroxide (V-$Ni(OH)_2$/NF) nanosheets array, which was further cleaned with water and ethanol, respectively. Finally, the nanosheets was fabricated by nitridation of the prepared cobalt doped nickel hydroxide nanosheets in a tube furnace system at 420 ℃ for 2h under the high purity NH_3 atmosphere which was named as V-Ni_3N. For comparison, the pure Ni_3N was also synthesized with similar procedure without adding NH_4VO_3 (denoted as Ni_3N/NF). V-Ni_3N-2 and V-Ni_3N-10 were obtained by varying the atomic ratios of V:Ni in the hydrothermal solution to 0.02:0.098 and 0.1:0.9, respectively. The corresponding commercial 20 wt% Pt/C powder were dipped on Ni foam for the comparison experiment.

Pt/C electrode as a reference was prepared by the following method: 21.5 mg of commercial Pt/C was mixed with 110 μl of deionized water, 106 μl of alcohol and 5 μl

of nafion to form a slurry, then which was dropped on the NF (1×1 cm^2) and dried at room temperature.

Cr-Ni_3N, Co-Ni_3N, Mn-Ni_3N, Mn-Ni_3N, W-Ni_3N and Fe-Ni_3N were synthesized by using $Cr(NO_3)_2 \cdot 9H_2O$, $Co(NO_3)_2 \cdot 6H_2O$, $Mn(NO_3)_2 \cdot 4H_2O$, Na_2MoO_4, Na_2WO_4 and $Fe(NO_3)_2 \cdot 9H_2O$, respectively. Transition metal doping can be adjusted by changing the type of transition metal salts. The molar ratio of transition metal salt to $Ni(NO_3)_2 \cdot 6H_2O$ is 0.05 mmol : 0.95 mmol. Other steps were the same as those for V-Ni_3N**.**

Materials characterization: To analyze the samples composition and microstructure, X-ray diffraction (XRD) was conducted on a PANalytical X'Pert Powder (Panalytical B.V.). Field-emission scanning electron microscopy (FESEM) analysis was performed on the JEOL JSM-7800F to characterize the surface morphologies. High-resolution transmission electron microscopy (HRTEM), high-angle annular dark-field scanning transmission electron microscopy (HAADF-STEM), and energy-dispersive spectroscopy (EDS) mapping were performed on the Talos F200S. X-ray photoelectron spectroscopy (XPS) experiments were performed on the ESCALAB250Xi, and all of the XPS binding energies were calibrated using the contaminant carbon (C1S) as a reference. Ultraviolet Photoemission Spectroscopy (UPS) experiments were collected at ThermoFisher ESCALAB 250Xi. Electron paramagnetic resonance (EPR) spectra were measured by Bruker A300 spectrometer at 20 °C.

Electrochemical measurement: All electrochemical measurements were performed on CHI660E electrochemical work station (Shanghai Chenhua Instrument

Co., Ltd., China) by using the typical three-electrode set-up at 25℃. V-Ni_3N/NF-5 was used directly as the work electrode (1 cm^{-2} electrode area), and a Hg/HgO electrode and a Pt plate served as the reference electrode and the counter electrode, respectively. For the HER in alkaline media, all the potentials were recorded with respect to the reversible hydrogen electrode (RHE) using equation ($E_{RHE} = E_{Hg/HgO} + 0.098 + 0.059$* pH), where E_{RHE} is the potential referred to RHE and $E_{Hg/HgO}$ is the practically applied voltage window. Linear sweep voltammograms (LSV) were tested at a scan rate of 2 mV s^{-1} in 1M KOH after 30 cyclic voltammetry (CV) testing. The onset potential was defined as the potential required when the current density of 1 mA cm^{-2}. Electrochemical impedance spectra (EIS) were recorded with a frequency ranging from 10^6 to 0.01 Hz and an amplitude of 5 mV at a fixed potential. The voltage is -100 mV vs. RHE. In HER measurements, all polarization curves were iRs-corrected (90%) using the equation: $E_{iRs\text{-}corrected} = E - iRs$, where E is the original potential, Rs is the solution resistance, i is the corresponding current, and $E_{iRs\text{-}corrected}$ is the iRs-corrected potential. The electrochemically active surface area (ECSA) was estimated by measuring the capacitive current associated with double-layer charging from scan-rate dependence of CVs and the scan rates were 20-60 mV s^{-1}. The polarization curves before and after cycling are recorded under quasi-equilibrium conditions at a scan rate of 2 mV s^{-1}. The capacitance current was measured within the potential range of the non-Faraday region.

Computational details: Plane-wave density functional theory (DFT) calculations were performed on CASTEP code of the Materials Studio package of Accelrys Inc. Generalized gradient approximation (GGA) in the form of Perdew–Burke–Ernzerhof

(PBE) functional was employed for the DFT exchange correlation energy and ultrasoft pseudo-potentials are used for the core electrons. A plane-wave basis set with an energy cutoff energy of 500 eV was assigned. The force atomic relaxation was 0.01 eV $Å^{-1}$. The Ni_3N (001) surface was modeled by a periodic five-layer slab repeated in 2×2 surface unit cell with a vacuum width of 10 Å between the slabs along the Z axis, where all atoms were fully relaxed. The water adsorption energy E_{H2O} is calculated by $E_{H2O} = E_{(surf+H2O)}-E_{(surf)} -E_{H2O}$, where $E_{(surf+ H2O)}$ and $E_{(surf)}$ are the total energies of the surface with and without the H_2O adsorbate, and $E_{(H2O)}$ is the energy of a free water molecule. Additionally, the hydrogen adsorption free energy $\triangle G_{H^*}$ is calculated by $\triangle G_{H^*} = E_{(surf+H)}-E_{(surf)}-1/2E_{(H2)}+\triangle E_{ZPE}-T\triangle S$, where $\triangle E_{ZPE}$ and $\triangle S$ are the difference in the zero-point energy and entropy between the adsorbed H atom and the gaseous phase H_2. At T=289.15 K, $\triangle G_{H^*}$ can be calculated by $\triangle G_{H^*} =E_{(surf+H)}-E_{(surf)}- 1/2E_{(H2)}+0.24$ eV.[1-3]

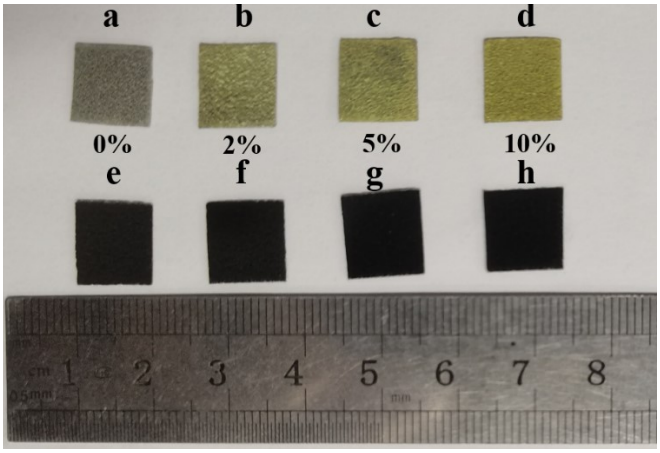

Figure S1. (a-d) Optical images of different samples after the hydrothermal reaction with different amounts of vanadium doping (0-10%). Optical images of Ni_3N (e), V-Ni_3N-2 (f), V-Ni_3N-5 (denoted as V-Ni_3N) (g), and V-Ni_3N-10 (h).

Interestingly, it shows that as the vanadium content increases, the color of the hydrothermal product gradually darkens, changing into light green, green, dark green and yellow-green.

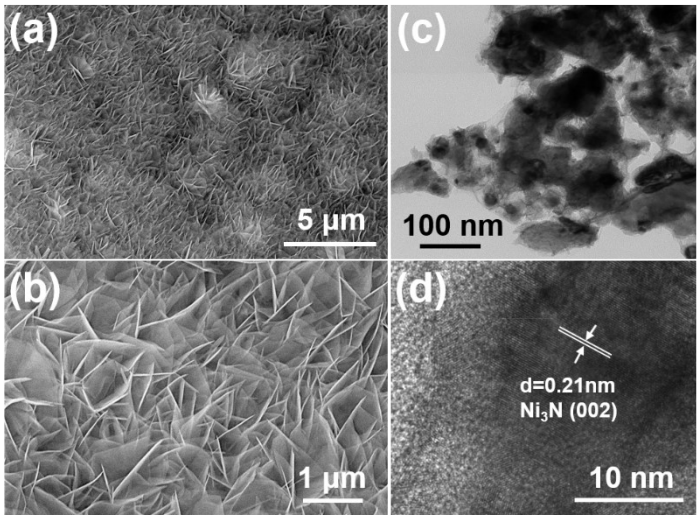

Figure S2. (a-b) SEM images of V-$Ni(OH)_2$/NF; TEM image (c) and HRTEM image (d) of V-Ni_3N nanosheets.

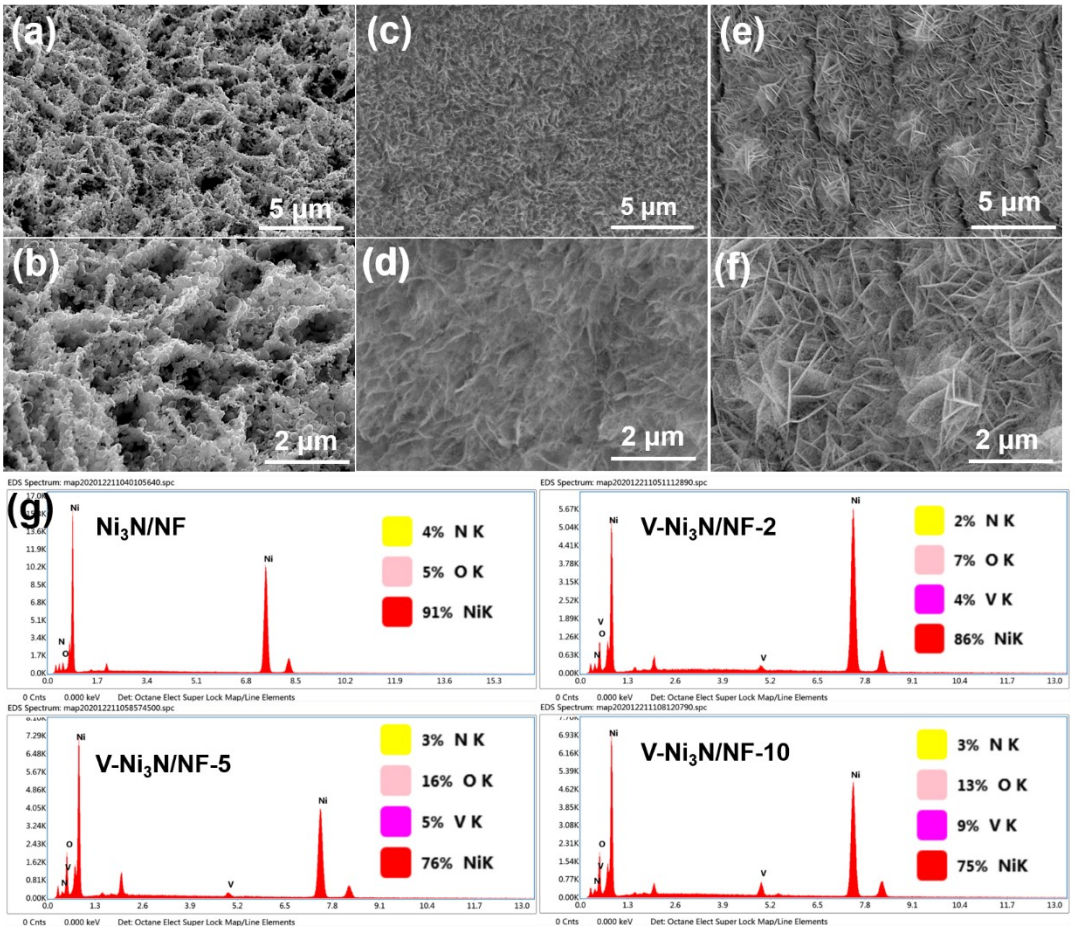

Figure S3. (a-b) SEM images of and Ni_3N; (c-d) SEM images of V-Ni_3N-2; (e-f) SEM images of V-Ni_3N-10. (g) Energy dispersive spectrometry (EDS).

After the nitridation process at 420 °C, the nanosheets structure of the catalysts with the doping amount of V of 0% and 2% collapsed to varying degrees. However, when the doping amount is increased to 5% and 10%, the catalysts inherit the excellent nanosheet morphology.

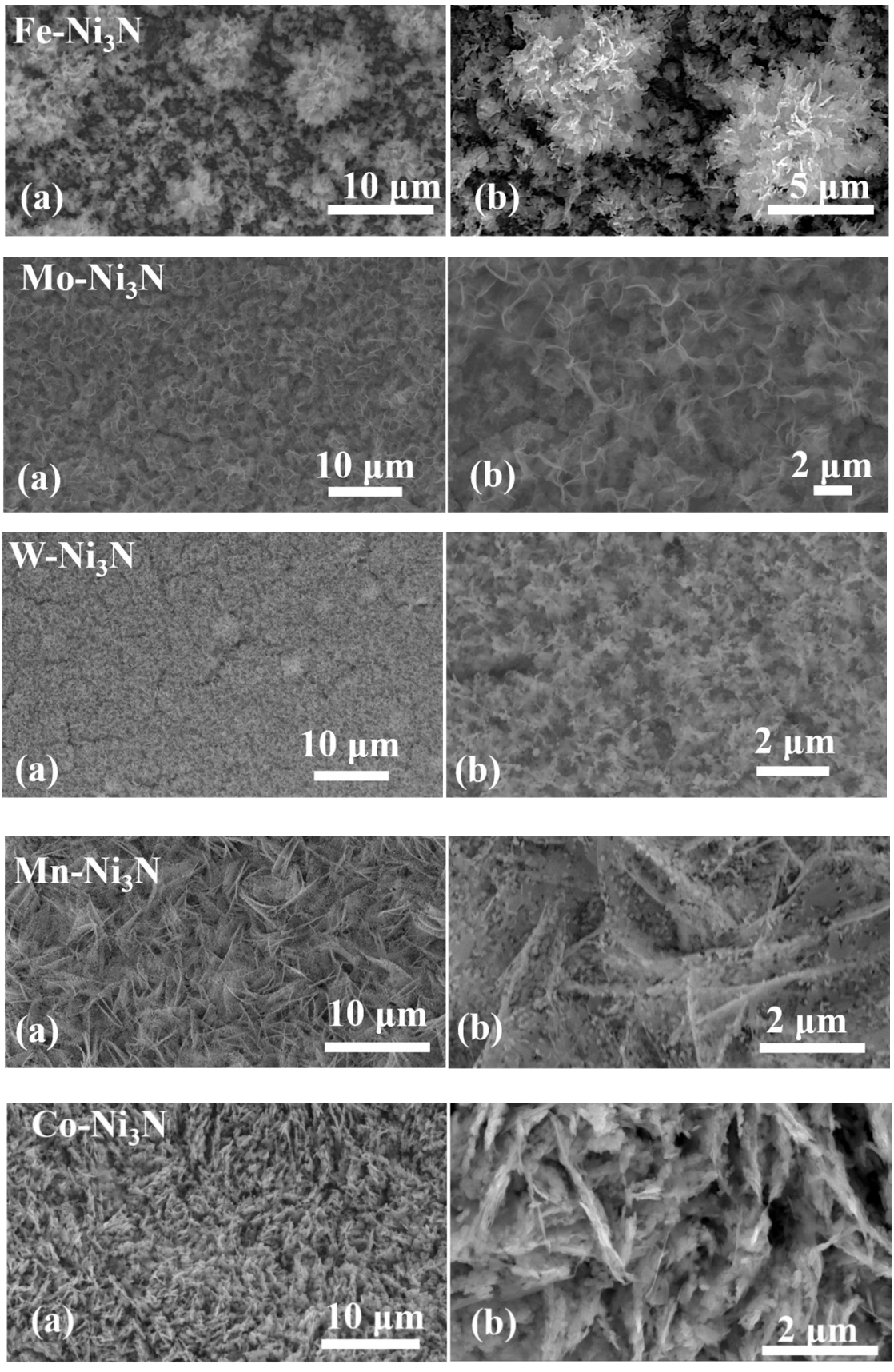
Fe-Ni3N
(a)
10 μm
(b)
5 μm
Mo-Ni3N
(a)
10 μm
(b)
2 μm
W-Ni3N
(a)
10 μm
(b)
2 μm
Mn-Ni3N
(a)
10 μm
(b)
2 μm
Co-Ni3N
(a)
10 μm
(b)
2 μm

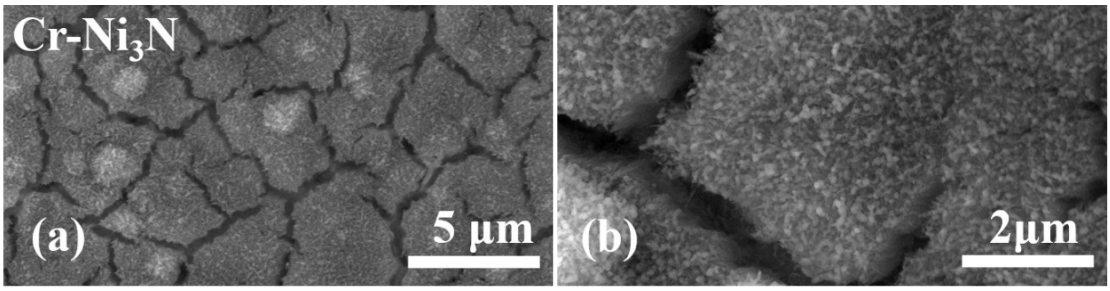

Figure S4. SEM images of transition metal doped Ni_3N, respectively.

As we can see in Fig. S4, different doped transition metals have different effects on the microstructure of Ni_3N. The hydroxides generated by the hydrothermal reaction are all in the form of nanosheets, and all the nanosheets show different degrees of collapse and sintering after annealing. For example, after annealing, the nanosheets of V-Ni_3N become thinner due to the removal of water molecules, and some tiny nanoparticles appear on the surface of the nanosheets. Similar to this are Co-Ni_3N and Mn-Ni_3N. Mo-Ni_3N exhibits nanosheet morphology similar to MoS_2. However, Cr-Ni_3N, Fe-Ni_3N and W-Ni_3N show some nanoparticle. In short, different transition metals have different physicochemical properties, so their effects on the morphology of Ni_3N are also different.

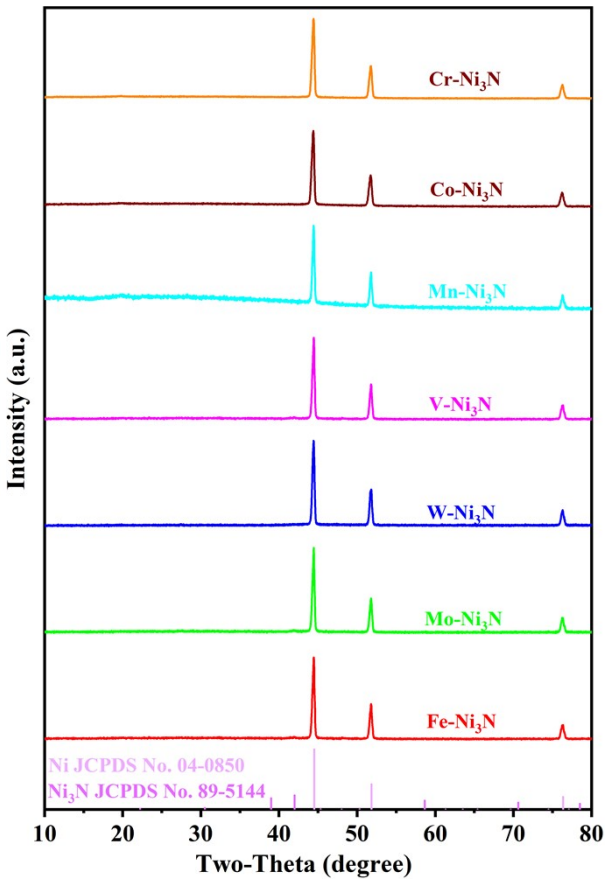

Figure S5. XRD patterns.

Table S1. Details of the crystal structures of Ni_3N, $Ni(OH)_2$, and Ni.

Samples	Crystal	Space group	*a* (Å)	*c* (Å)
Ni_3N (JCPDS No.89-5144)	Hexagonal	P6322(182)	4.616	4.298
$Ni(OH)_2$ (JCPDS No.73-1520)	Hexagonal	P-3m1 (164)	3.114	4.617
Ni (JCPDS No.04-0850)	Cubic	Fm-3m(225)	3.524	3.524

Table S2. Elemental content of V-Ni_3N.

Element	Atomic Fraction
V	4.1
Ni	76.6
N	19.3

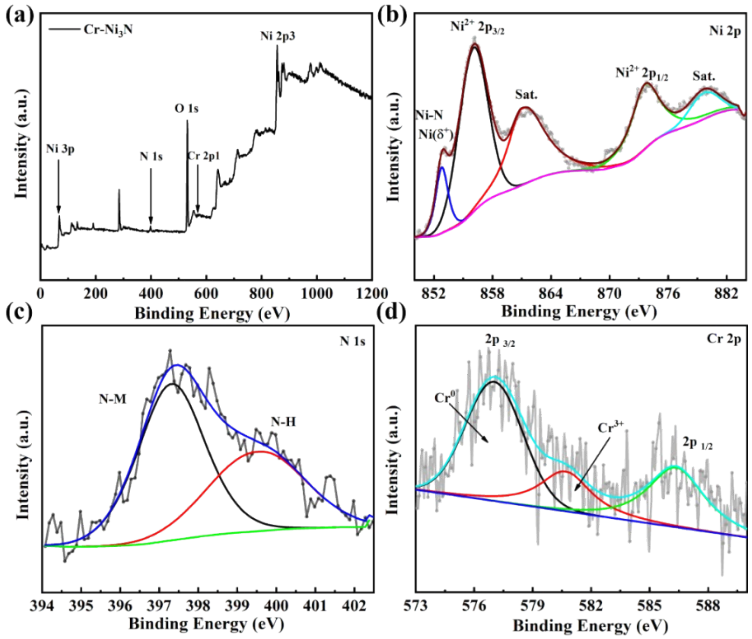

Figure S6. XPS survey spectrums of Cr-Ni_3N; High-resolution XPS spectra of Ni (b), N (c) and Cr (d).

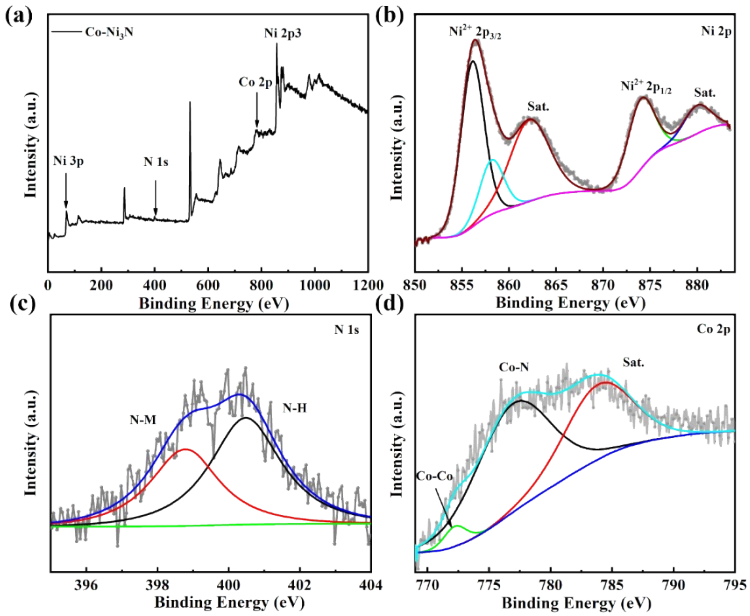

Figure S7. XPS survey spectrums of Co-Ni_3N; High-resolution XPS spectra of Ni (b), N (c) and Co (d).

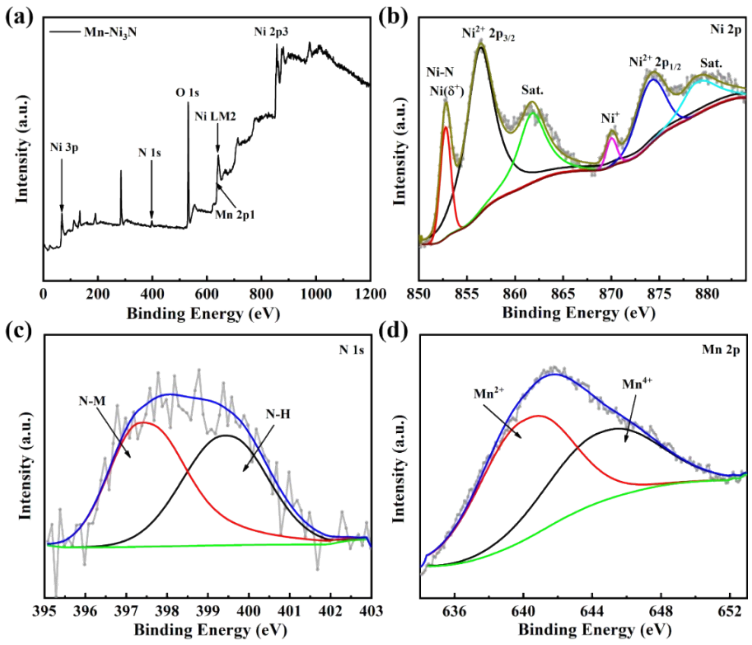

Figure S8. XPS survey spectrums of Mn-Ni_3N; High-resolution XPS spectra of Ni (b), N (c) and Mn (d).

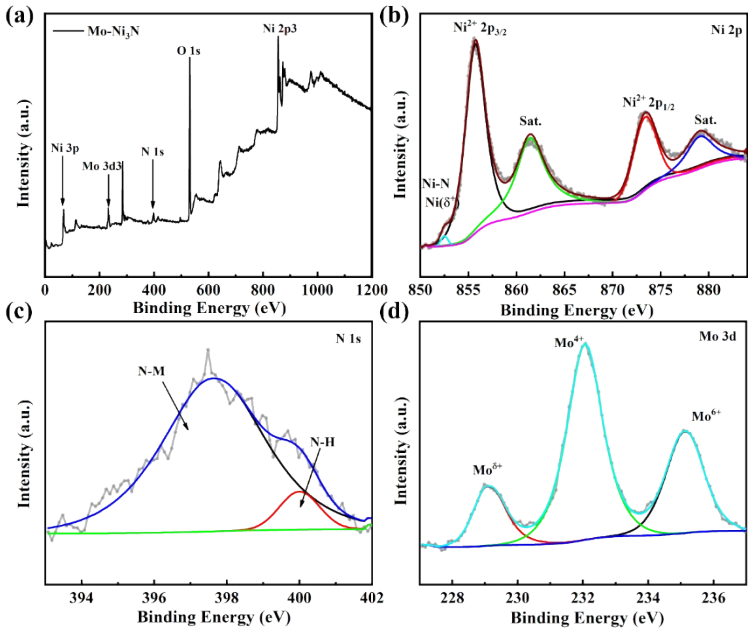

Figure S9. XPS survey spectrums of Mo-Ni_3N; High-resolution XPS spectra of Ni (b), N (c) and Mo (d).

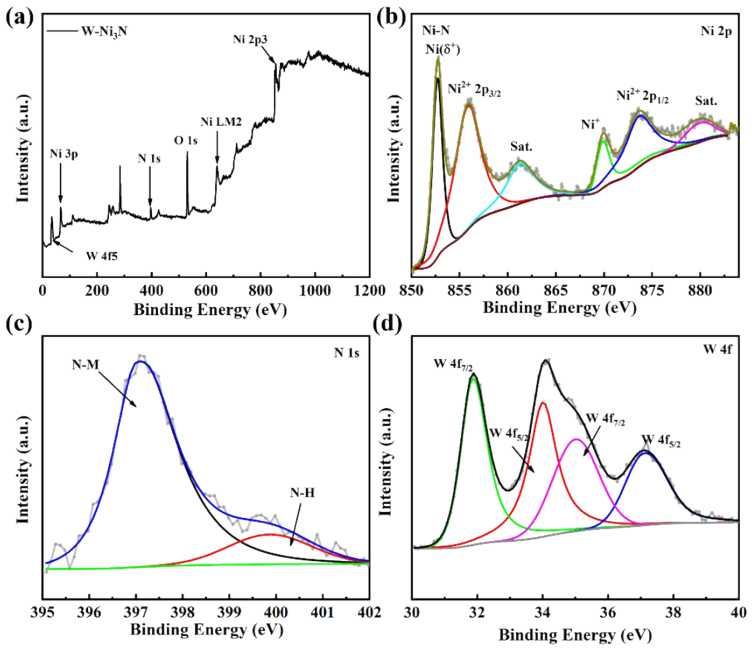

Figure S10. XPS survey spectrums of W-Ni_3N; High-resolution XPS spectra of Ni (b), N (c) and W (d).

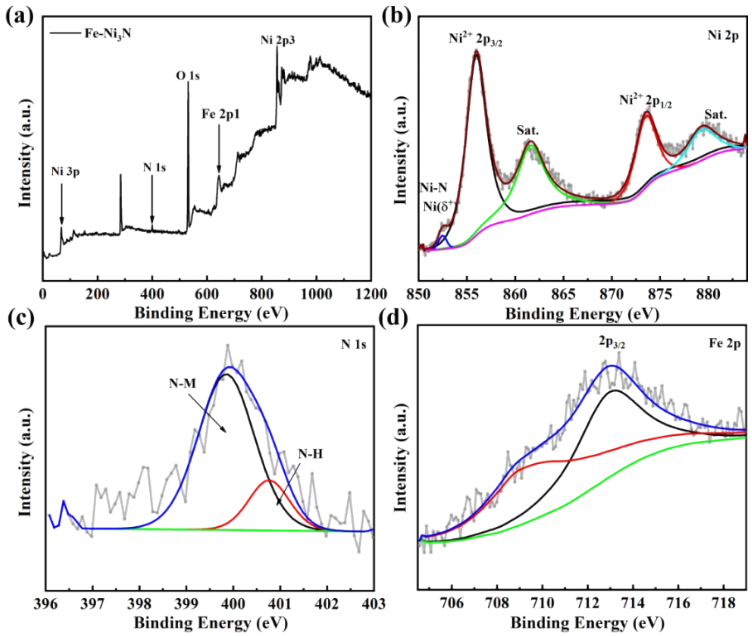

Figure S11. XPS survey spectrums of Fe-Ni_3N; High-resolution XPS spectra of Ni (b), N (c) and Fe (d).

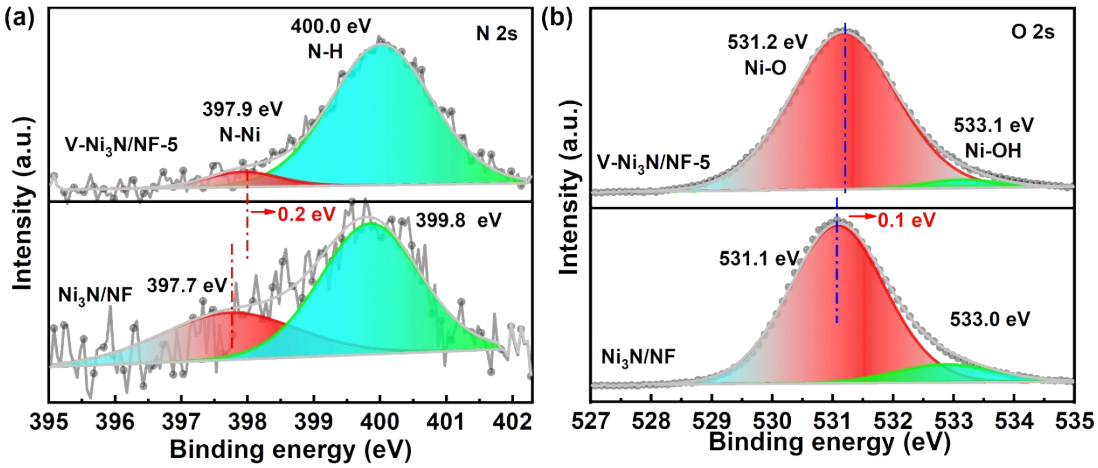

Figure S12. (a) High-resolution N 2s XPS spectra, and (b) High-resolution O 2s XPS spectra.

The positive shift of N 2s and O 1s peak in V-Ni_3N/NF-5 relative to that for Ni_3N/NF corroborated the efficient electron transfer after V doping and altered surface charge state.

Table S3. Elemental content of V-Ni_3N.

Element	**Atomic Fraction**
V	5.2
Ni	94.8

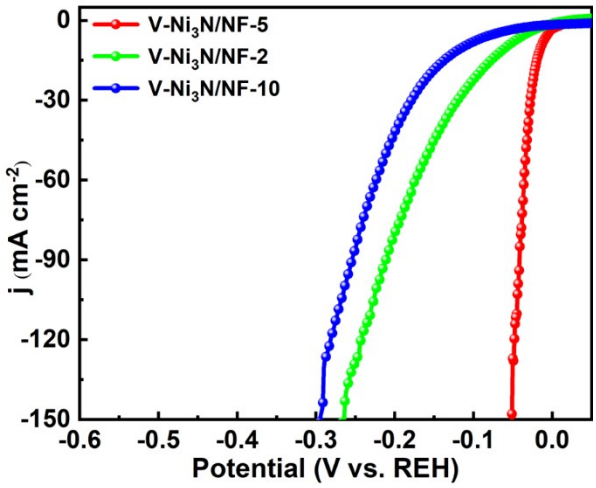

Figure S13. LSV curves of V-Ni_3N/NF-5, V-Ni_3N/NF-2, and V-Ni_3N/NF-10 for HER.

The experiments with different doping levels were also carried out to get an optimized condition (**Figure S13**). We found that the V-Ni_3N/NF-5 (denoted as V-Ni_3N) shows the highest activity, characterized by the lowest overpotentials, and smallest R_{ct}. Meanwhile, the experimental results show that as the amount of vanadium increases, the C_{dl} of the material increases.

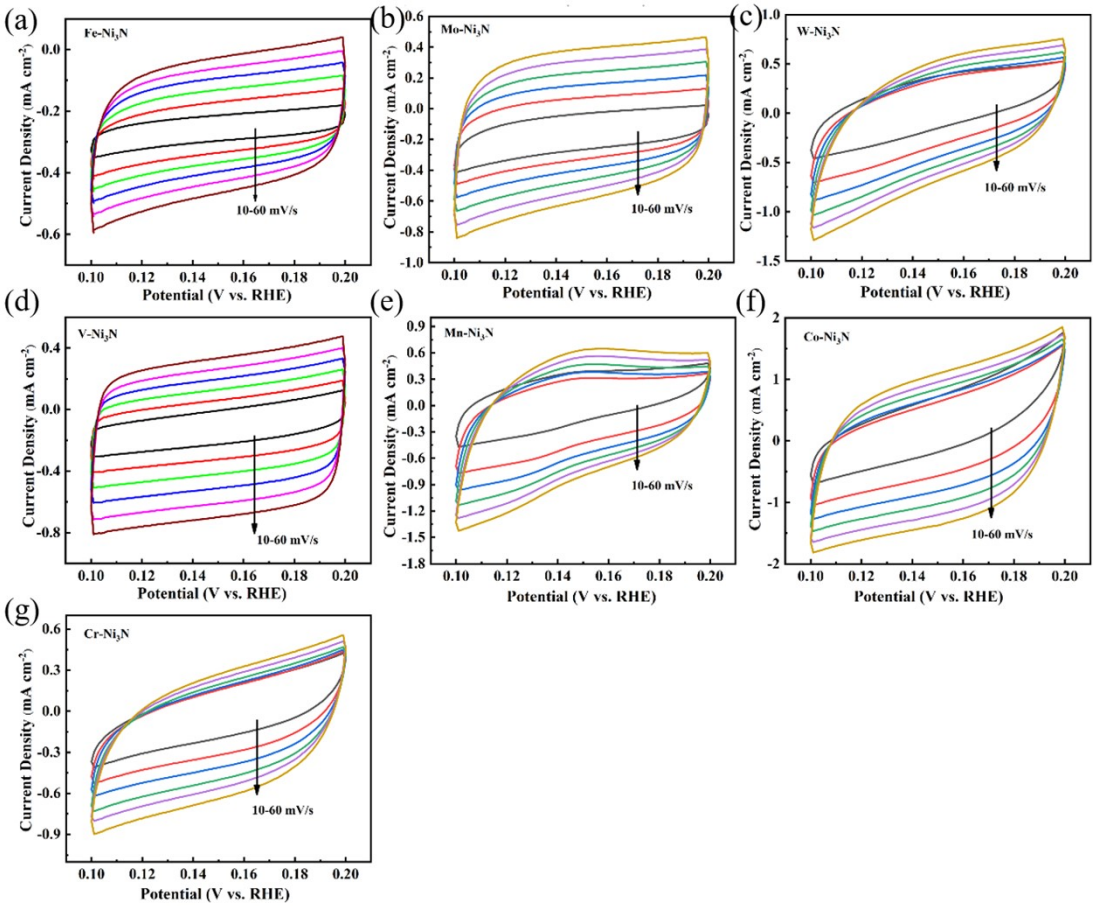

Figure S14. Cyclic voltammetry curves recorded in 1 M KOH at scan rates of 10, 20, 30, 40, 50 and 60 mV s^{-1}.

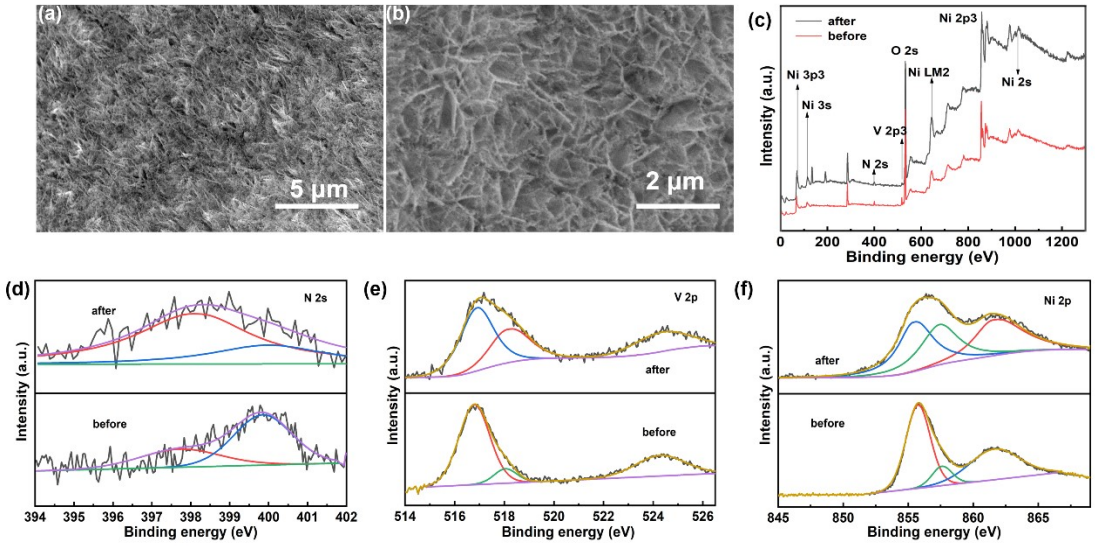

Figure S15. (a-b) SEM images of the catalyst after electrochemical test. (c-f) XPS survey spectrum and high-resolution XPS spectra of V-Ni_3N/NF-5.

The analysis reveals that the macroscopic morphology and valence states of the elements on the surface of V-Ni_3N have no significant changes, which further proves that the catalyst has excellent catalytic stability and corrosion resistance.

Table S4. Sample masses after different processing stages.

Sample	Mass of substrate (mg)	Sample area (cm^2)	Mass density (mg cm^{-2})
V-Ni_3N/NF-5	**37.2**	**1*1*2=2**	**1.85**
V-Ni_3N/NF-10	**35.6**	**1*1*2=2**	**1.05**
V-Ni_3N/NF-2	**37.6**	**1*1*2=2**	**2.04**
Ni_3N/NF	**36.7**	**1*1*2=2**	**1.6**
V-$Ni(OH)_2$/NF	**35.1**	**1*1*2=2**	**0.8**
NF	**33.5**	**1*1*2=2**	**-**

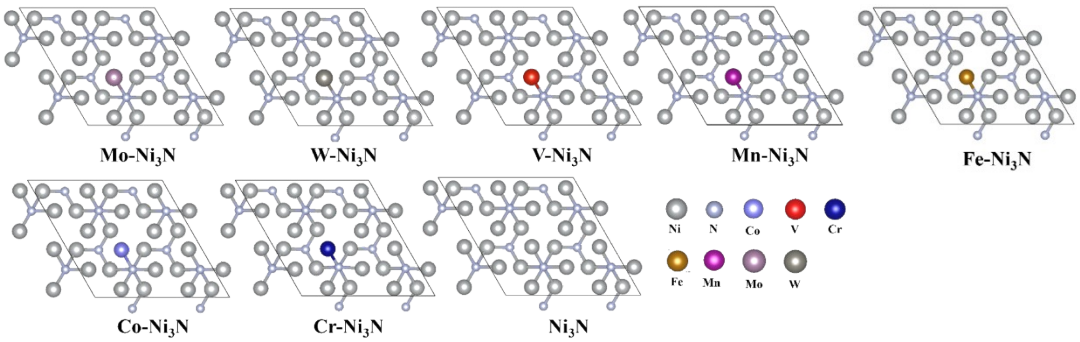

Figure S16. Optimized calculation model constructed by replacing Ni with corresponding transition metal elements.

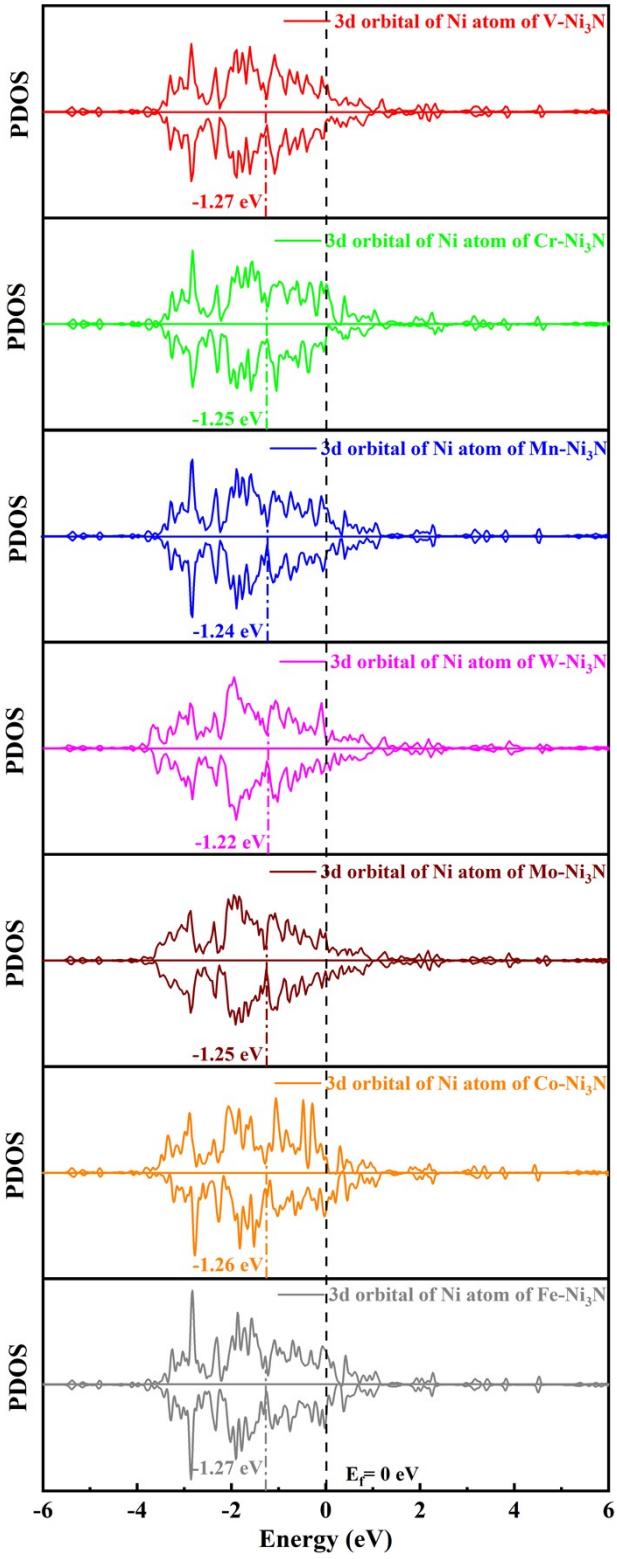

Figure S17. D-band center of catalysts.

Table S5. Comparison of the overpotentional at 10 mA cm^{-2} with recently reported other electrocatalysts.

Catalysts	**Electrolytes**	**η_{10} (mV)**	**Tafel slope ($mV\ dec^{-1}$)**	**Reference**
Ru-Ni_3N	1M KOH	51	55	Chem Eng J 2023;451:138698
Ni_3N/NF	1M KOH	45	97	Int J Hydrog Energy 2021;46:27037-27043
Ni_3N/Ni@C750	1M KOH	172	63	Int J Hydrog Energy 2021;46:30739-30749
Ni_3N/W_5N_4	1M KOH	31	34	Appl Catal B: Environ 2022;307:121198
Ir-Ni_3N	1M KOH	66.7	66.76	Appl Surf Sci 2023;637:157896
Ni_3N-Co_3N/C	1M KOH	58	70.2	Appl Catal B: Environ 2021;297:120461
Mn-NiS_x/NiO/Ni_3N@NF	1M KOH	93	113	Appl Surf Sci 2023;619:156789
Ni_3N-V_2O_3	1M KOH	53	63	Chem Eng J 2021;415:128864
Ni_3N/Mo_2N	1M KOH	20	33.8	ACS Catal 2023;13:4091-4100

Ni_3N/NF	1M KOH	121	109	Electrochimica Acta 2016;191:841.
Co-Ni_3N	1M KOH	30	41.6	J Phys Chem Lett 2021;12(6):1581-1587.
NiMo HNRs/Ti mesh	1M KOH	92	76	J Mater Chem A 2015;3:20056.
Ni_3N-VN/NF	1M KOH	64	37	Adv Mater 2019;31(23):1901174.
Ru/Ni_3N–Ni	1M KOH	53	32.4	Chem Commun 2020;56(15):2352-2355.
Ni/Co_2N	1M KOH	16.2	60.5	ACS Appl Mater Interfaces 2020;12:29357-29364.
Fe-Ni_3C-2% nanosheets	1M KOH	292	43	Angew Chem Int Ed 2017;56:12566.
Epitaxial in-growth Co-Ni_3N	1M KOH	194	156	Adv Mater 2018;30(13):1705516.
MOF-Derived Ni_3N	1M KOH+0.5M Urea	47	67	ACS Sustainable Chem Eng 2020;8(19):7414-7422.
V doped Co_4N	1M KOH	37	44	Angew Chem Int Ed 2018;57(18):5076-5080.

Ni_3N/C	1M KOH	64	48	Angew Chem Int Ed 2019;58(22):7445-7449.
N-Ni	1M KOH	96	N/A	J Am Chem Soc 2017;139:12283.
MoO_3/Ni–NiO	1M KOH	62	59	Adv Mater 2020;32(39):2003414.
High-Valance State Doped Ni_3N	1M KOH	Mo:12 W:40 V:10	64 118 110	ACS Catal 2019;9:9332−9338.
CeO2/Co4N	1M KOH	30	66	Appl Catal B: Environ 2020;277:119282.
RuNi-NCNFs	1M KOH	35	30	Adv Sci 2020;7:1901833.
Co-Mo_5N_6	1M KOH	19	12	Adv Energy Mater 2020;10:2002176.
This work	1M KOH	15	28.7	-

References

[1] D, Merki, S. Fierro, H. Vrubel and X. Hu, Amorphous molybdenum sulfide films as catalysts for electrochemical hydrogen production in water, *Chem. Sci.*, 2011, **2**, 1262-1267.

[2] H. Jin, H. Zhang, J. Chen, S. Mao, Z. Jiang and Y. Wang, A general synthetic approach for hexagonal phase tungsten nitride composites and their application in the hydrogen evolution reaction, *J. Mater. Chem. A*, 2018, **6**, 10967-10975.

[3] E. J. Popczun, J. R. McKone, C. G. Read, A. J. Biacchi, A. M. Wiltrout, N. S. Lewis and R. E. Schaak, Nanostructured nickel phosphide as an electrocatalyst for the hydrogen evolution reaction, *J. Am. Chem. Soc.*, 2013, **135**, 9267-9270.